Journal of Materials Chemistry A

RSC Publishing

PAPER

View Article Online
View Journal | View Issue

Cite this: J. Mater. Chem. A, 2013, 1, 5709

Mesoporous silicon@carbon composites *via* nanoparticle-seeded dispersion polymerization and their application as lithium-ion battery anode materials†

Juchen Guo,‡* Zichao Yang and Lynden A. Archer*

Received 27th November 2012
Accepted 18th March 2013

DOI: 10.1039/c3ta01272g

www.rsc.org/MaterialsA

Significant efforts have been devoted to synthesis and characterization of engineered silicon nanostructures able to withstand the large stresses and strains produced by lithium alloying/dealloying reactions during electrochemical cycling. Less attention has been given to ensuring robust connection between silicon and its host structure in the anode. The current work develops a new methodology to create nanocomposites in which silicon nanoparticles are uniformly dispersed in a mesoporous carbon host. The composite is synthesized through copolymerization of acrylonitrile and silicon nanoparticles densely functionalized with vinyl groups, which serve as seeds for free radical dispersion polymerization, followed by carbonization of the PAN coating/network. The method yields nanocomposites with high, reversible capacities and stable cycling performance.

Introduction

Silicon is arguably the most promising anode material for lithium-ion batteries (LIBs) for its high Li storage capacity and low lithiation/delithiation potential *vs.* Li/Li^+. It is broadly recognized that the greatest challenge for implementation of a commercial lithium ion battery based on a Si anode is the fast capacity fading, induced by the drastic volume change the material undergoes during electrochemical cycling. Despite sustained efforts in the past decade to eliminate this shortcoming, development of a practical Si anode remains a significant research challenge. One-dimensional materials including pure Si wires,[1–7] carbon coated Si wires or tubes,[8,9] and Si coated carbon nanotubes[10–13] possess an inherent mechanism for relaxing cyclic stresses produced by Li insertion and show the greatest promise to date. A recent study by Cui and coworkers demonstrated SiO_x/Si double-walled nanotubes that showed extraordinary performance over 6000 charge–discharge cycles with 85% capacity retention.[14] However, achievement of low-cost mass-producible Si anodes that exhibit acceptable levels of cycling stability is still elusive. A number of previous studies show that when the characteristic dimension of Si structures in the anode are small enough (approximately 150 nm in diameter for spheres and 100 nm in diameter for wires and tubes), pulverization of Si should not occur, even in an anode cycled through fully lithiated and delithiated states.[15,16] This conclusion contradicts data, which show persistent capacity fading in LIB anodes, even though the majority of materials used in these studies have dimensions quite well below the calculated critical sizes.

An emerging opinion is that persistent capacity fading observed in Si anodes is not solely the result of mechanical instability of the Si nanostructures. Rather, it is hypothesized that degradation of the connections between the Si active material and its supportive and conductive surroundings may be to blame. This process can be induced by local strains and stresses produced by the material's volume change during electrochemical cycling in a battery electrode. In this sense, to improve the cycling stability of Si anodes may require greater efforts targeted at improving the stability of the bonds used to integrate the Si active material in its surroundings in the anode. A rational design for the Si anode may therefore be to construct the anode based on uniformly embedded individual Si active material (in whatever morphology as long as the primary structures are small enough to prevent the pulverization) into a resilient and conductive framework that is able to bond strongly to the Si material even as it undergoes large volume changes. Obtaining a uniform dispersion of Si active material in the framework is a key factor in practical realization of such a system.

To date, only a few studies have used the above concept to engineer Si anodes.[17–20] Cho *et al.* for example reported micron-sized Si–C particles with porous nanostructure synthesized using an organic Si precursor and SiO_2 particles as sacrificial

School of Chemical and Biomolecular Engineering, Cornell University, Ithaca, NY 14853, USA. E-mail: laa25@cornell.edu; jguo@engr.ucr.edu

† Electronic supplementary information (ESI) available. See DOI: 10.1039/c3ta01272g

‡ Current address: Department of Chemical and Environmental Engineering, University of California at Riverside, Riverside, CA 92521, USA.

templates; Yushin *et al.* reported Si–C composite particles prepared by CVD deposition of Si in a porous carbon framework. Both studies demonstrated Si-based anodes with excellent cycling stability. A drawback of these works however is that the synthesis procedures are complicated and expensive, and are thus unlikely to be of practical commercial interest. In this study, we demonstrate a novel route to synthesize uniformly structured mesoporous Si–C composites using inexpensive materials under mild reaction conditions.

Experimental

Materials synthesis

All chemical reagents were purchased from Sigma-Aldrich, unless otherwise specified, and used without additional purification. Commercial silicon nanoparticles (SiNPs) with average diameters ranging from 20 to 30 nm were purchased from Nanostructured & Amorphous Materials, Inc. (see TEM image in ESI Fig. S1†) and co-functionalized with hydrophilic and vinyl groups to create water-dispersible, polymerizable seeds for dispersion free-radical polymerization. Hairy nanoparticles in which polyacrylonitrile was tethered to the SiNPs were produced by dispersion polymerization of acrylonitrile. Upon removal of the water, these particles spontaneously formed SiNP@PAN nanocomposites in which the SiNPs were homogeneously dispersed in an interconnected PAN network. Thermal treatment carbonized PAN and created the desired micron-sized mesoporous Si–C nanocomposites in which Si particles were dispersed in a carbon matrix.

The pristine SiNPs were cleaned in piranha solution (a mixture of concentrated sulfuric acid and 30% hydrogen peroxide solution with a 3 : 1 volume ratio) by moderate stirring for 1 h, and then washed with an adequate amount of water to neutral pH. In addition to cleaning the surface, this method introduced a thin, coherent oxide film on the particle surfaces to permit subsequent attachment of a PAN layer. 500 mg of the as-prepared SiNPs were dispersed in 200 mL of 1 M ammonium hydroxide aqueous solution with moderate stirring and sonication for 30 min. The obtained SiNPs dispersion was centrifuged at 8000 rpm for 20 min. The precipitate was removed and a clear SiNP suspension with a light yellow color was obtained. The SiNP concentration was determined as 1.5 mg mL^{-1} by gravimetric analysis. 200 mg of 3-(trimethoxysilyl)propyl methacrylate (MPS) was dissolved in 2 mL of ethanol, and the MPS solution was slowly added in 100 mL of the obtained SiNP suspension with a syringe pump in a span of 8 h under vigorous stirring at room temperature, and the mixture was continuously stirred for a total of 48 h. MPS was added in excess to ensure sufficient grafting on SiNP surface.[21] Based on the particle size of the SiNP, the ratio between MPS and SiNP was estimated as 15 μmol MPS per m^2 of SiNP. The resulting MPS-grafted SiNP (MPS–SiNP) suspension was dialyzed against adequate amount of water until the pH became approximately 8.

To prepare seeds for dispersion polymerization, 115.5 mg of sodium dodecyl sulfate (SDS), 107.5 mg of potassium persulfate (KPS), and 2.5 g of acrylonitrile (AN) were added to 100 mL of MPS–SiNP suspension. The molar concentrations of SDS, KPS, and AN were 4 mM, 4 mM, and 0.47 M, respectively. The mixture was stirred at room temperature for 10 min to obtain a homogenous suspension, which was transferred into a three-necked flask equipped with condenser and purged with N_2 gas for 30 min. The polymerization was started by immersing the flask into an oil bath at 70 °C while under vigorous stirring and N_2 protection. The reaction was stopped after 18 h by quenching in an ice bath. The solution after the polymerization was slightly translucent and retained the light yellow color of the starting aqueous SiNP–water dispersion.

Characterization

The crystal structures of the products were characterized using Scintag Theta-theta PAD-X X-Ray Diffractometer (Cu Kα, λ = 1.5406 Å). Their morphologies were studied using FEI Tecnai G2 T12 Spirit Transmission Electron Microscope (120 kV). Thermogravimetric analysis was performed using TA Instruments Q5000 IR Thermogravimetric Analyzer. Raman spectra were collected using a Renishaw InVia Confocal Raman Microscope (laser wavelength = 488 nm). Nitrogen adsorption analysis was performed with a Micromeritics ASAP 2020 Accelerated Surface Area and Porosimetry System.

Electrochemical characterization

Electrochemical characterization of the SiNP@C nanocomposites as anode materials in rechargeable lithium batteries was performed at room temperature in 2032 coin-type cells. The working electrode consisted of 92 wt% of the SiNP@C particles and 8 wt% PVdF as binder; no carbon conductivity aid was added. The loading of SiNP@C in the tested anodes was in a range of 0.85 mg cm^{-2} to 1.1 mg cm^{-2}. Copper foil (0.004 in. thick, Alfa Aesar) was used as the current collector. Lithium foil (0.03in thick, Alfa Aesar) was used as the counter and reference electrode. 1 M $LiPF_6$ in a mixture of ethylene carbonate, dimethyl carbonate, and diethyl carbonate (1 : 1 : 1 volume ratio) was used as the electrolyte. Celgard 2500 polypropylene membranes were used as the separator. Assembly of cell was performed in a glove box with moisture and oxygen concentrations below 0.1 ppm. The room-temperature electrode capacities were measured using Neware CT-3008 battery testers (The accuracy of the batter tester is ±0.001 mA and ±2.5 mV) and cyclic voltammetry (CV) was performed with a Solartron Model 1470 Potentiostat/Galvanostat.

Results and discussion

The morphology of the SiNP@PAN particles was characterized by transmission electron microscopy (TEM) as shown in Fig. 1. Compared with the pristine SiNPs, the SiNP@PAN particles show distinctly different morphology. Specifically, the size of SiNP@PAN particles is larger (~50 nm) than the precursor SiNPs and the surfaces of the particles are visibly rough. The rough surface is thought to originate from the reasonable solubility (7.35 wt%) of AN monomer in water, which results in low interfacial energy between water and the PAN corona. Similar particle morphologies have been observed in AN–styrene

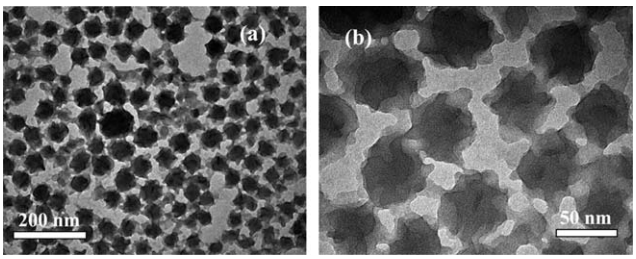

Fig. 1 TEM images of the SiNP@PAN particles network at different magnifications.

emulsion copolymerization.[22] The solubility of AN in water also results in the formation of connective PAN filaments that link the SiNP@PAN particles as clearly seen in Fig. 1(b).

The surfactant sodium dodecyl sulfate (SDS) is used in the synthesis to stabilize the growth process of the SiNP@PAN particles. The concentration of SDS plays a critical role in achieving SiNP@PAN particles with the desired morphology. When propagation of the PAN chains begins on the SiNP surface, the increasing surface tension is thought to attract SDS molecules in solution to the interface, which prevents massive particle aggregation. This beneficial attribute of SDS is, however, offset by the fact that if its concentration rises above the critical micelle concentration (CMC), undesirable free micelles will spontaneously form in the water phase. It was observed that when the SDS concentration is increased to 6 mM, which is close to its (CMC ≈ 8 mM) in water, pure PAN particles were formed in the dispersion in addition to SiNP@PAN particles (see Fig. S2†). This likely arises from the fact that AN oligomers stabilized by the SDS micelles in the water phase provide additional polymerization loci that compete with the growing SiNP@PAN particles for AN monomer. As an extreme illustration, the same dispersion polymerization reaction was carried out without the MPS–SiNP seeds. The obtained PAN particles are seen to have distinctly different morphologies, as expected (see TEM image in ESI Fig. S3†).

After polymerization, the SiNP@PAN particles were harvested by freeze-drying the solution. The resulting SiNP@PAN powder was heated in air at 300 °C (the melting temperature of PAN) for 30 min, at which point the temperature was raised to 900 °C and maintained there for 1 h under argon purge. The purpose of the heat treatment at 300 °C in air was to facilitate relaxation of the PAN chains and to facilitate rearrangement of the PAN host structure to promote the dehydrogenation reaction of PAN. X-ray diffraction scans of the pristine SiNPs after heat treatment in air at 600 °C and after the piranha treatment are provided in Fig. 2(a) and (b). Both XRD patterns are consistent with expectations for polycrystalline silicon. In contrast, the XRD patterns for the SiNP@C composite (Fig. 2(c)) show none of the sharp peaks characteristic of crystalline silicon and instead only two broad peaks centered at 2θ values near 25° and 45°, consistent with partially graphitic carbon. The XRD patterns also show no evidence of SiC in the SiNPs at any stage of the synthesis, implying that the absence of crystalline Si peaks is not a consequence of carbonation of the SiNPs. Fig. 3(a) and (b) are the corresponding Raman spectra for the SiNP after the piranha wash and for the SiNP@C composite. The strong Raman band at around 520 cm^{-1} seen in Fig. 3(a) is characteristic for polycrystalline Si. The two weaker, less well defined Raman bands at 300 cm^{-1} and at 900 cm^{-1} have been observed in an earlier report for Si@SiO_x composites,[23] and in the present case is probably due to the native SiO_2 and oxide coating produced during the piranha treatment.

Fig. 3(b) shows that none of these features remains in the Raman spectrum for the SiNP@C composite. Instead, Fig. 3(b) shows two Raman bands characteristic of disordered graphite and amorphous carbon. Deconvolution of the Raman spectrum in Fig. 3(b) the 800–2000 cm^{-1} range indicates that the carbon in the composite consists of approximately 15.1% graphite (G), 68.9% disordered graphitic lattices (D1) and 16.0% amorphous carbon (D3). The absence of any of the Raman bands expected for crystalline Si in the composite may confirm the amorphous nature of the Si after the surface functionalization, polymerization, and carbonation steps, which has been observed in other nanometer-sized Si–C composites.[24] It may also reflect the fact that the SiNPs are surrounded by a dense carbon layer. The first explanation though consistent with the results from XRD, cannot explain the complete disappearance of Raman bands for SiO_x apparent in Fig. 3(b). This observation is in fact consistent with the idea that a dense carbon coating attenuates the exciting laser light and Raman scattering from the carbon and SiO_x encapsulated SiNP core.

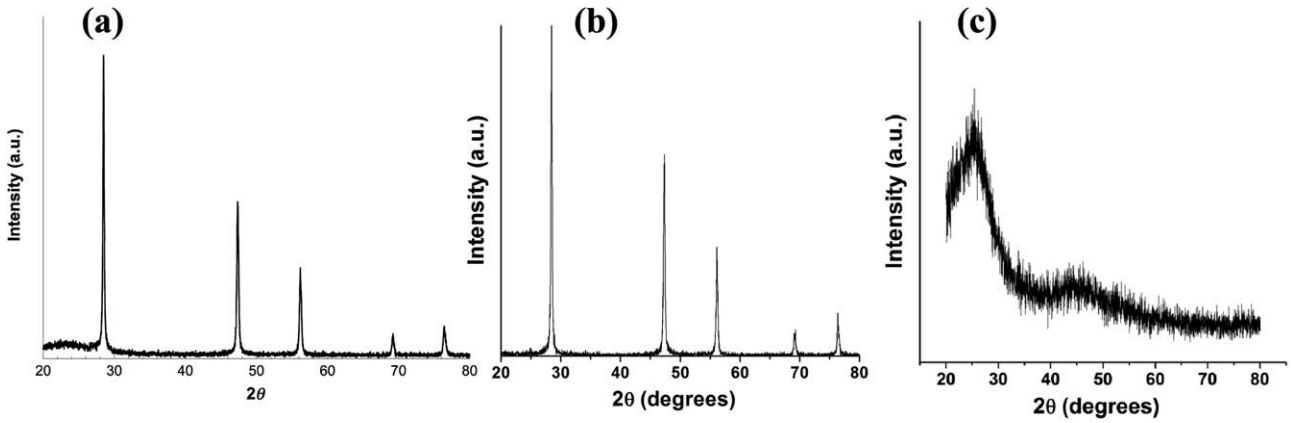

Fig. 2 XRD patterns for: (a) pristine SiNPs heated in air for 2 h at 600 °C; (b) SiNPs after cleaning with piranha solution; (c) final SiNP@C nanocomposite.

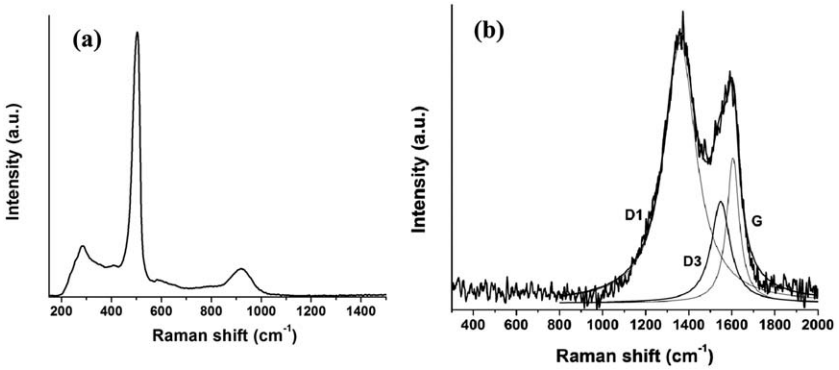

Fig. 3 Raman spectra for: (a) SiNP cleaned with piranha solution and (b) final SiNP@C nanocomposite.

TEM images of SiNP@C composite are shown in Fig. 4(a) and (b). Fig. 4(a) clearly indicates the self-assembly of the micron-sized and rod-shaped SiNP@C nanocomposite particles. EDX analysis (Fig. 4(c) and (d)) confirms the presence of silicon in the SiNP@C composite. The significant oxygen content revealed by EDX analysis likely reflects the sustained presence, after carbonization, of the slioxane bridges used to anchor the MPS to the Si particles and partial oxidation of the SiNPs. The transparent appearance of the SiNP@C nanocomposite and the results from high magnification TEM image in Fig. 4(b) are both consistent with the mesoporous nature of the SiNP@C particles, which is further confirmed by the nitrogen adsorption results shown in Fig. 5(a) and (b). This indicates that most of the pores in the carbon lie in the size range of 2–40 nm. The BET surface area of the composite is 52 m^2 g^{-1}, which corresponds to a surface area of 52/(1–56%) = 118 m^2 g^{-1} for the carbon in the composite, assuming the contribution to surface area is all from carbon.

To evaluate the electrochemical properties of the mesoporous SiNP@C nanocomposites, the material was tested in two-electrode coin cells using Li metal foil as the counter electrode. Thermogravimetric analysis (see ESI Fig. S4†) indicate that the SiNP content in the SiNP@C particles is 56 wt%. To simplify comparisons with previous reports and to assess the true promise of the SiNP@C composites as electrode materials, all capacities reported herein are for the total SiNP@C mass in the electrodes, *i.e.* not only for the *ca.* 56 wt% of SiNP in the composites. Fig. 6(a) shows the delithiation capacity and coulombic efficiency (CE) of the SiNP@C anode as functions of cycle number under a current density of 200 mA g^{-1} (~C/5) between 1.5 V and 0 V *vs.* Li/Li^+. The lithiation capacity of the SiNP@C anode in the 1st cycle is 3570 mA h g^{-1}. However, the delithiation capacity in the 1st cycle is only 795 mA h g^{-1}, which makes the CE in the 1st cycle only 22.3%. The undesirable low CE may be a result of the irreversible electrochemical reduction of the oxidized SiNPs in the first lithiation reaction.

After the first cycle, the delithiation capacity gradually increases (activation), and the CE also quickly improves. After 20 cycles, the delithiation capacity is seen to stabilize at 1110 mA h g^{-1}, and the CE at this point is 91.7%. After 115 cycles, the delithiation capacity is 1010 mA h g^{-1}. The CE reaches 100% at the 70th cycle and remains constant thereafter. The initial low CE likely reflects the initial irreversible reaction of SiO_x species in the composite particles. The rise in CE observed with increasing cycle number is consistent with the geometric configuration of the composites, wherein the SiO_x layer is more accessible to Li^+ ions in the electrolyte than the active, buried Si material. As SiO_x is deliberately introduced to anchor the carbon precursor (PAN) to the SiNPs and to

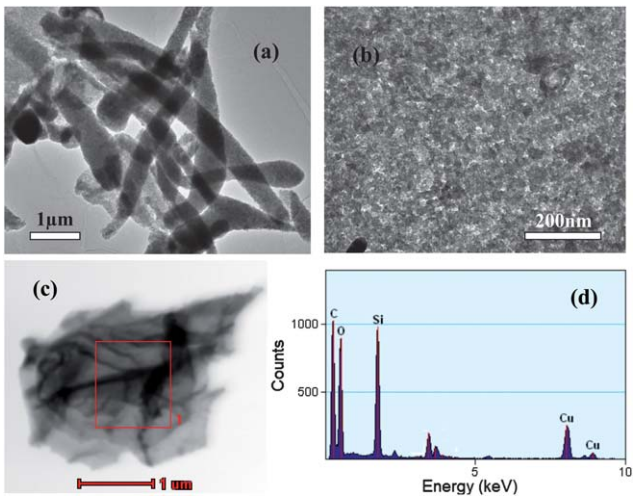

Fig. 4 (a) and (b) TEM images of the SiNP@C mesoporous composite at different magnifications; (c) STEM image of SiNP@C composite; (d) EDX spectrum based on the square area in (c).

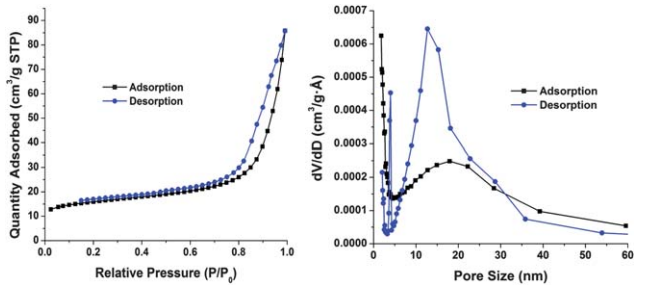

Fig. 5 Nitrogen adsorption isotherms and pore size distribution of the SiNP@C nanocomposites.

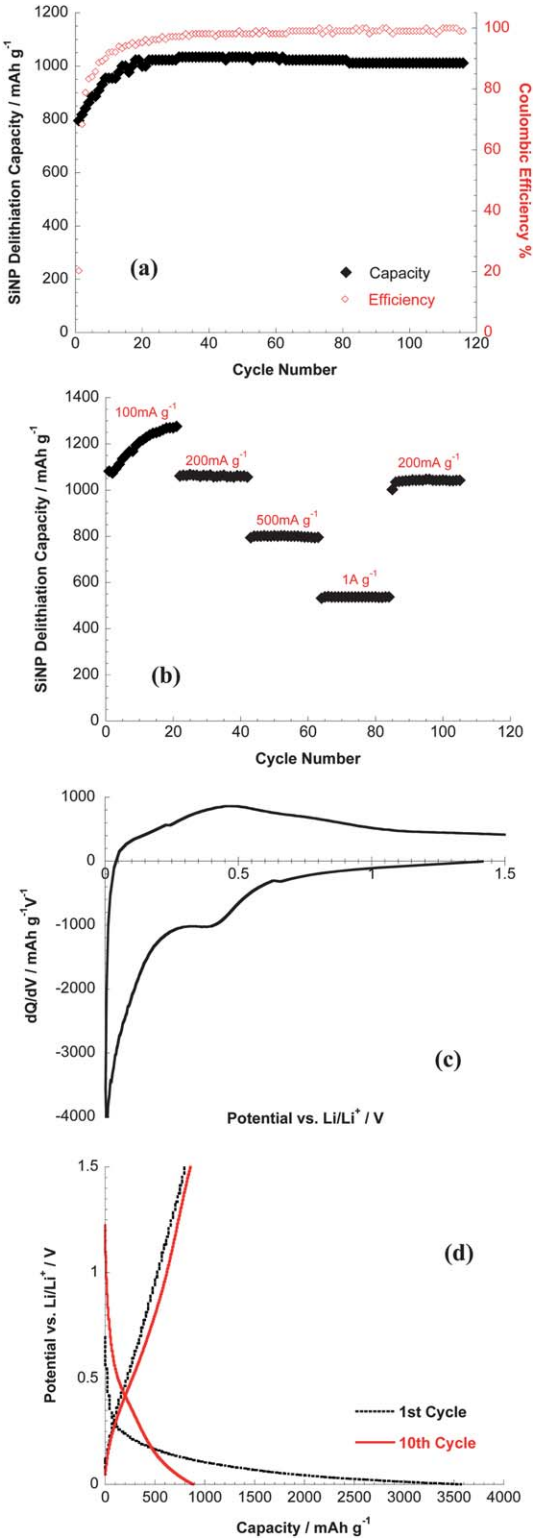

Fig. 6 (a) Reversible delithiation capacity and coulombic efficiency for SiNP@C/Li half cells; (b) specific capacity *versus* rate for SiNP@C/Li half cells; (c) differential capacity curve at a rate of 0.5 mV s^{-1} of the SiNP@C particles obtained from cyclic voltammetry; (d) charge–discharge curve for the 1st and the 10th cycle for the mesoporous SiNP@C particles.

homogeneously disperse the SiNPs in PAN, it may be impossible to eliminate the initially low CE values and their rise with cycle number. A potential remedy under active investigation is to replace MPS with short polyethylene glycol-methyl acrylate (PEGMA) as the initiator for dispersion polymerization of AN. This change would remove the need for the SiO_x anchoring layer and the high curvature of the SiNPs should lead to their homogeneous dispersion in PAN of moderate molecular weights.[25]

The rate capability of the materials was also evaluated using galvanostatic cycling measurements under various cycling rates of C/10 (100 mA g^{-1}), C/5 (200 mA g^{-1}), C/2 (500 mA g^{-1}), 1C (1 A g^{-1}), and back to C/5. The SiNP@C composites demonstrate attractive rate capability and retain a capacity of 520 mA h g^{-1} at a 1 A g^{-1} current density. The differential capacity curve (Fig. 6(c)) shows two lithiation peaks at 0.4 V and 0.1 V, and a broad delithiation peak at 0.5 V, which is consistent with typical Si anode materials. Efforts are underway to fine-tune the polymerization and carbonization conditions to create optimal nanocomposites with higher SiNP contents to increase the overall anode capacity. However, it can be shown that used in conjunction with current lithiated LIB cathodes,[26] Si-based anodes with the capacities reported herein already provide optimal specific energies.

Fig. 6(d) reports the charge–discharge voltage profiles for the 1st and the 10th cycles. The 1st lithiation curve shows a slope-shaped plateau below 0.3 V, which is not consistent with the plateau normally observed for polycrystalline Si. The highly sloped lithiation profile seen in the first cycle indicates that the large irreversible capacity in the 1st cycle may be attributed to the partially oxidized SiNPs. The absence of a clear plateau in the profiles recorded in subsequent cycles is a feature of the materials that demands improvement, but is similar to what has been reported in earlier studies using amorphous SiO_x and silicon monoxide materials as LIB anodes.[23,27] We suspect the source in the present case may be the disordered nature of the Si in the NPs, but cannot rule out a reversible contribution to the overall capacity from SiO_x species present in the SiNP@C composites.

Conclusions

We have synthesized micron-sized SiNP@C composite materials with mesoporous structure through an inexpensive, aqueous dispersion polymerization method. To our knowledge, the nanoparticle-seeded dispersion polymerization of PAN demonstrated in the study has heretofore not been reported. The size of the obtained SiNP@C particles are in micrometer size scale, which is favorable for Li-ion battery electrode manufacture due to the higher tap density and better safety features. Significantly, we find that when evaluated as lithium battery electrodes, the composites manifest excellent cycling stability and high reversible capacity. These characteristics can be attributed to the unique mesoporous structure enabled by the self-assembly of the SiNP@PAN particles during carbonization. Future studies will focus on improving the low initial CE and shape of the voltage profiles of the SiNP@C particles,

which appears to result from oxidization of SiNPs and/or from complete disordering of Si in the NPs during the final stages of the synthesis.

Acknowledgements

This material is based on work supported as part of the Energy Materials Center at Cornell, an Energy Frontier Research Center funded by the U.S. Department of Energy, Office of Science, Office of Basic Energy Sciences under Award Number DESC0001086. This work made use of the electron microscopy facility at the Cornell Center for Materials Research (CCMR), an NSF supported MRSEC through Grant DMR-1120296.

Notes and references

1 C. K. Chan, H. Peng, G. Liu, K. McIlwrath, X. Zhang, R. A. Huggins and Y. Cui, *Nat. Nanotechnol.*, 2008, **3**, 31.
2 L. Cui, R. Ruffo, C. K. Chan, H. Peng and Y. Cui, *Nano Lett.*, 2009, **9**, 491.
3 B. Laik, L. Eude, J.-P. Pereira-Ramos, C. S. Cojocaru, D. Pribat and E. Rouviere, *Electrochim. Acta*, 2008, **53**, 5528.
4 R. Huang, X. Fan, W. Shen and J. Zhu, *Appl. Phys. Lett.*, 2009, **95**, 133119.
5 W. Xu and J. C. Flake, *J. Electrochem. Soc.*, 2010, **157**, A41.
6 K. kang, H. Lee, D. Han, G. Kim, D. Lee, G. Lee, Y. Kang and M. Jo, *Appl. Phys. Lett.*, 2010, **96**, 053110.
7 H. T. Nguyen, F. Cao, M. R. Zamfir, C. Biswas, K. P. So, Y. H. Lee, S. M. Kim, S. N. Cha, J. M. Kim and D. Pribat, *Adv. Energy Mater.*, 2011, **1**, 1154.
8 C. K. Chan, R. N. Patel, M. J. O'Connell, B. A. Korgel and Y. Cui, *ACS Nano*, 2010, **4**, 1443.
9 M. Park, M. Kim, J. Joo, K. Kim, J. Kim, S. Ahn, Y. Cui and J. Cho, *Nano Lett.*, 2009, **9**, 3844.
10 L. Cui, Y. Yang, C. Hsu and Y. Cui, *Nano Lett.*, 2009, **9**, 3370.
11 W. Wang and P. N. Kumta, *ACS Nano*, 2010, **4**, 2233.
12 L. Hu, H. Wu, Y. Gao, A. Cao, H. Li, J. McDough, X. Xie, M. Zhou and Y. Cui, *Adv. Energy Mater.*, 2011, **1**, 523.
13 K. Evanoff, J. Khan, A. A. Balandin, A. Magasinski, W. J. Ready, T. F. Fuller and G. Yushin, *Adv. Mater.*, 2012, **24**, 533.
14 H. Wu, G. Chan, J. W. Choi, I. Ryu, Y. Yao, M. T. McDowell, S. W. Lee, A. Jackson, Y. Yang, L. Hu and Y. Cui, *Nat. Nanotechnol.*, 2012, **7**, 310.
15 M. H. Park, K. Kim, J. Kim and J. Cho, *Adv. Mater.*, 2010, **22**, 415.
16 X. Liu, L. Zhong, S. Huang, S. Mao, T. Zhu and J. Huang, *ACS Nano*, 2012, **6**, 1522.
17 H. Kim and J. Cho, *Nano Lett.*, 2008, **8**, 3688.
18 H. Kim, B. Han, J. Choo and J. Cho, *Angew. Chem., Int. Ed.*, 2008, **47**, 10151.
19 A. Magasinki, P. Dixon, B. Hertzberg, A. Kvit, J. Ayala and G. Yushin, *Nat. Mater.*, 2010, **9**, 353.
20 H. Jia, P. Gao, J. Yang, J. Wang, Y. Nuli and Z. Yang, *Adv. Energy Mater.*, 2011, **1**, 1036.
21 E. Bourgeat-Lami and J. Lang, *J. Colloid Interface Sci.*, 1998, **197**, 293.
22 K. Landfester and M. Antonietti, *Macromol. Rapid Commun.*, 2000, **21**, 820.
23 Y.-S. Hu, R. Demir-Cakan, M.-M. Titirici, J.-O. Muller, R. Schlogl, M. Antonietti and J. Maier, *Angew. Chem., Int. Ed.*, 2008, **47**, 1645.
24 J. Saint, M. Morcrette, D. Larcher, L. Laffont, S. Beattie, J.-P. Peres, D. Talaga, M. Couzi and J.-M. Tarascon, *Adv. Funct. Mater.*, 2007, **17**, 1765.
25 S. Srivastava, P. Agarwal and L. A. Archer, *Langmuir*, 2012, **8**, 6276.
26 U. Kasavajjula, C. Wang and A. J. Appleby, *J. Power Sources*, 2007, **163**, 1003.
27 T. Park, J. Yeo, S. Jang, J. Miyawaki, I. Mochida and S. Yoon, *Nanotechnology*, 2012, **23**, 355601.

